



ROYAL INSTITUTE  
OF TECHNOLOGY

# Dynamics of Galaxy Clusters

When Dark Matter speaks, do Baryons listen?

JOEL JOHANSSON

Master's Thesis  
Dark Cosmology Centre  
The Royal Institute of Technology  
Supervisor: Steen H. Hansen  
External supervisor: Mark Pearce

TRITA xxx yyyy-nn



# DYNAMICS OF GALAXY CLUSTERS

by

JOEL JOHANSSON



*MASTER THESIS*

*at*



*Niels Bohr Institute  
University of Copenhagen  
December 18th 2008*

**SUPERVISOR:**

**STEEN H. HANSEN**

*Dark Cosmology Center  
University of Copenhagen*

# Abstract

Galaxy clusters are the most massive gravitationally bound structures in the universe (typically containing hundreds of galaxies), and have a great importance as cosmological probes of structure formation and dark matter in the universe.

Most of the cosmological applications rely on accurate measurements of cluster masses, which are hard to measure in observations.

One of the most used methods of mass measurements is based on observations of the X-ray emitting gas that pervades clusters. Traditionally, the total mass distribution is determined using only the radial density and temperature distributions of the intracluster medium under the assumption of spherical symmetry and hydrostatic equilibrium.

Comparing the X-ray-determined masses with other independent methods (such as gravitational lensing and numerical simulations) suggests that masses are typically underestimated by about 10-20%. This implies that substructure, dynamical effects (velocity anisotropies, bulk motion, turbulence etc.) might be significant.

In this thesis, we will for the first time attempt to measure the velocity component of the clusters, by allowing a departure from hydrostatic equilibrium (allowing radial and rotational motion). We will do this by applying the Euler equation and the Jeans equation to X-ray data.

# Contents

## Contents

<b>1</b>	<b>Introduction</b>	<b>1</b>
1.1	Observational Evidence of Dark Matter . . . . .	1
1.1.1	Cosmic Microwave Background . . . . .	2
1.1.2	Large Scale Structure . . . . .	2
1.1.3	Clusters of galaxies . . . . .	4
1.1.4	Galaxies . . . . .	5
1.2	Dark matter on all scales . . . . .	6
<b>2</b>	<b>Theory</b>	<b>7</b>
2.1	Fluid mechanics . . . . .	7
2.1.1	Continuity equation . . . . .	7
2.1.2	Euler's equation . . . . .	7
2.2	Jeans equations for spherical systems . . . . .	8
2.3	Spherical systems . . . . .	9
2.3.1	Spherically symmetric matter distributions . . . . .	10
2.4	Analytical models . . . . .	10
2.4.1	Dark matter density models . . . . .	10
2.4.2	Gas density models . . . . .	11
2.4.3	Temperature models . . . . .	12
2.4.4	Velocity anisotropy models . . . . .	12
2.5	Temperature of Dark matter . . . . .	13
2.6	Considerations on the cluster dynamics . . . . .	15
2.6.1	Radial motion . . . . .	16
2.6.2	Tangential motion . . . . .	17
<b>3</b>	<b>X-ray Observations of Clusters</b>	<b>19</b>
3.1	Physics of the Intracluster Medium . . . . .	19
3.2	X-ray analysis . . . . .	20
3.3	Calculating the radial velocity dispersion . . . . .	23
3.3.1	$\beta = \text{constant}$ . . . . .	23
3.3.2	$\beta = \beta(r)$ . . . . .	24

3.4	Inferring the velocity component . . . . .	25
3.4.1	Tangential motion . . . . .	27
3.4.2	Radial motion . . . . .	28
3.5	Conclusion and future improvements . . . . .	29
<b>Appendices</b>		<b>30</b>
<b>A Geometrical Deprojection</b>		<b>31</b>
<b>B Navier-Stokes equation</b>		<b>33</b>
<b>C Selection of analysed clusters</b>		<b>35</b>
C.1	RXJ1347.5 . . . . .	35
C.2	A1914 . . . . .	36
C.3	A2218 . . . . .	37
<b>Bibliography</b>		<b>39</b>

# Chapter 1

## Introduction

### 1.1 Observational Evidence of Dark Matter

The need of dark matter has been known since 1933, when Fritz Zwicky applied the virial theorem to the Coma cluster. After measuring the radial velocities of  $\sim 30$  cluster galaxies, he assumed that the Coma cluster was a spherically symmetric and 'mechanically stationary system' (Zwicky, 1937 [27]) that obeyed

$$2\langle T \rangle = -\langle V \rangle \quad \Rightarrow \quad 2 \frac{m_{gal} (3\sigma_r^2)}{2} = \frac{Gm_{gal}M_{tot}(< r)}{r} \quad (1.1)$$

where  $m_{gal}$  is the mass of a galaxy at radius  $r$  enclosing the total cluster mass  $M_{tot}(< r)$  and the radial velocity dispersion,  $\sigma_r = \langle (v_r - \langle v_r \rangle)^2 \rangle^{1/2}$ . An estimate of the total cluster mass is

$$M_{tot} \sim \frac{3r\sigma_r^2}{G} \approx 10^{15} M_{\odot} \left( \frac{r}{1.5 \text{ Mpc}} \right) \left( \frac{\sigma_r}{1000 \text{ km/s}} \right)^2 \quad (1.2)$$

Zwicky realised that the luminous galaxies could only contribute to  $\sim 10\%$  of the total cluster mass, and the lack of observational evidence for any non-luminous matter was the birth of the 'missing mass problem'. Proposed solutions followed four broad categories: *(i)* the virial theorem is not valid for these systems, *(ii)* other laws of physics (modified gravity models, such as MOND), *(iii)* non-luminous baryonic matter (like MACHO's) or *(iv)* non-baryonic dark matter.

Since then, the existence and nature of dark matter has been confirmed using a whole smörgåsbord of observational techniques, spanning many scales of structure size. The following sections will give a brief summary of how dark matter acts on different scales.

### 1.1.1 Cosmic Microwave Background

The existence of dark matter is seen at the largest scale possible - namely the size of the whole universe. The Cosmic Microwave Background (CMB) and the pronounced features of the CMB power spectrum are tightly related to the cosmological parameters, which are today measured with great precision.

If the matter content of the universe was purely baryonic, one would expect the temperature fluctuations of the CMB to be of the order  $\Delta T/T \sim 10^{-3}$  to explain the structures that we observe today (Hu, W. 1995 [12]). Temperature fluctuations of this level were long sought for, and it was not until 1992 the *Cosmic Background Explorer* (COBE) finally observed the CMB to be a nearly perfect blackbody spectrum of temperature  $T = 2.725$  K with small temperature anisotropies  $\Delta T/T \sim 10^{-5}$ . This can only be accounted for by non-baryonic dark matter that does not interact electromagnetically, allowing dark matter structures to form before decoupling without leaving a direct imprint on the temperature.

The amount of dark matter has a significant effect on the CMB angular power spectrum (left panel fig. 1.1). The interplay between dark matter and baryons in the hot plasma changes the structure of the acoustic peaks. The best fit to the data is the  $\Lambda$ CDM model, which has a baryonic fraction  $f_b = \Omega_b/\Omega_m = 0.17$ .

We therefore know that there exists about five times more dark matter than baryonic matter on the scale of the entire universe.

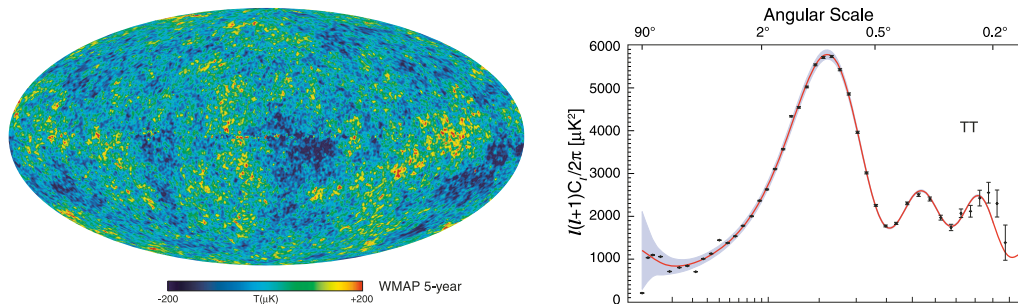


**Figure 1.1.** Left: The CMB temperature fluctuations observed over the full sky by the *Wilkinson Microwave Anisotropy Probe* (WMAP). The average temperature is 2.725 K. Red regions are warmer and blue regions are colder by  $\sim 0.0002$  degrees. Right: The angular power spectrum of the CMB describes how much the temperature fluctuates on different angular scales. The highest peak (angular size  $\sim 1^\circ$ ) is the first acoustic peak. (NASA/WMAP Science Team, 2008 [10])

### 1.1.2 Large Scale Structure

Different cosmologies predict different large-scale structures for the universe. By studying how mass is distributed in the universe and how structures evolve in time,

## 1.1. OBSERVATIONAL EVIDENCE OF DARK MATTER

we can understand even more about the nature of dark matter than what we have already learned from the CMB.

For instance, Hot Dark Matter (HDM) ('hot' refers to particles travelling with relativistic velocities) would be able to stream out of the potential wells of overdense regions in the early universe, dampening the formation of dense objects such as dark matter halos (a speed of a few hundred km/s is sufficient to escape from a galaxy halo, thereby erasing structure on that scale). In the HDM scenario, structure formation would proceed 'top-down', with the largest structures forming first, then fragmenting into smaller structures like clusters or galaxies.

With Cold Dark Matter (CDM) ('cold' refers to particles travelling with non-relativistic velocities), structure formation would proceed 'bottom-up' (hierarchically), by merging of smaller objects into larger objects (galaxies  $\rightarrow$  groups  $\rightarrow$  clusters).

Spectroscopic redshift surveys like the *2-degree-Field Galaxy Redshift Survey* (2dFGRS), CfA2 and the *Sloan Digital Sky Survey* (SDSS) measure the spatial distribution of galaxies, and how this distribution evolves with time. Fig. 1.2 shows that the observed galaxy distribution of the universe is in good agreement with mock galaxy distributions constructed using the Millennium Simulation of large-scale structure based on  $\Lambda$ CDM cosmology.

Accordingly, we have strong reasons to believe in the  $\Lambda$ CDM paradigm, as it puts further constraints on the nature of dark matter and how structure formation proceeds.

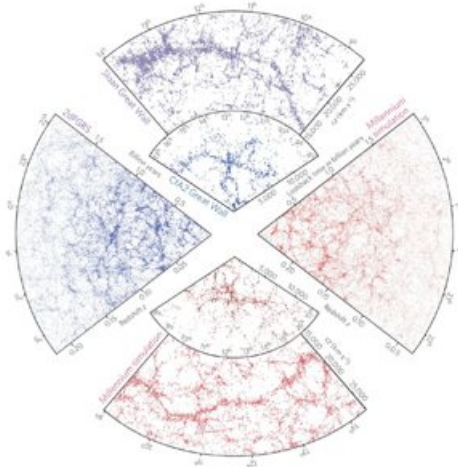


**Figure 1.2.** Large-scale galaxy distribution in the universe obtained from surveys (CfA2,2dFGRS,SDSS) (blue) compared with mock galaxy distribution from the Millennium simulation (red). The Millennium Simulation shows that  $\Lambda$ CDM cosmology reproduces the same web-like features (voids, filaments) as observed in the real universe. (Springel et al., 2006 [25])

### 1.1.3 Clusters of galaxies

Clusters of galaxies are the largest gravitationally bound structures in the universe ( $\sim 10^{15} M_{\odot}$  within 2 Mpc of their centers). They formed by gravitational collapse around rare peaks of the primeval density field, on scales of the order  $\sim 10$  Mpc. Thus, the number density of galaxy clusters probes the cosmic evolution of large-scale structure and provides an effective test of different cosmological models. Because of the large collapse scale, the cluster gas fraction  $f_{gas} = M_{gas}/M_{tot}$  is expected to be close to the cosmic value  $\Omega_b/\Omega_m = 0.17 \pm 0.01$ .

The mass distribution within clusters also provides information of cosmological use, and can be measured through many complementary methods:

(i) The motions of individual galaxies can be used to trace the cluster potential. Dynamical analysis using the virial theorem typically derive mass-to-light ratios,  $\Upsilon \simeq 200 - 300 (M_{\odot}/L_{\odot})$  (Sarazin 1986 [24]; Binney&Tremaine 2008 [1]). Assumptions on the dynamical state of the cluster have to be made, since this method is sensitive for systematic uncertainties due to velocity anisotropies, substructure and projection effects.

(ii) Distortion of background galaxies by gravitational lensing offers a method for measuring projected masses of clusters. Cluster cores are dense enough to produce strong gravitational lensing, creating multiple distorted images (arcs) of background galaxies. Further away from the core, weak gravitational lensing imprint a tangential shear pattern of background galaxies. The lensing methods are free from assumptions about the dynamical state of the cluster, but uncertainties in redshift distribution of lensed background galaxies and projection effects complicate three-dimensional mass distributions.

(iii) Measurements of the X-ray emissivity and temperature of the hot cluster gas provide good estimates of the total mass distribution, traditionally done by using the hydrostatic Euler equation, which implies certain assumptions about the dynamical state of the cluster (to be discussed in glorious detail in following chapters). X-ray measurements typically give gas fractions  $f_{gas} \sim 0.13$ . Mass estimates from strong lensing (within  $r < 200$  kpc of the cluster center) generally agree with X-ray determined masses. On larger scales ( $r > 0.5$ Mpc), weak lensing, X-ray and dynamical mass measurements show fair agreement (Allen et. al 2001). Comparing X-ray observations with simulations of galaxy clusters shows that the hydrostatic equilibrium method typically underestimates masses by  $\sim 10$ - $20\%$ , indicating that neglect of dynamical effects might be significant (Piffaretti&Valdarnini 2008 [22]; Nagai et al. 2007 [18]).

(iv) The thermal Sunyaev-Zeldovich (tSZ) effect arises as the CMB radiation shines through the hot plasma in galaxy clusters. Inverse Compton scattering will boost CMB photons to higher frequencies and distort the Planck blackbody spectrum. The tSZ effect typically yield  $f_{gas} \sim 0.12$  (Laroque et al. 2006 [15])

The kinetic Sunyaev-Zeldovich (kSZ) effect is a second-order effect. Just as the thermal motions of ICM electrons can up-scatter the CMB photons, bulk motion

## 1.1. OBSERVATIONAL EVIDENCE OF DARK MATTER

(peculiar velocities in regard to the Hubble flow and/or turbulent motions) can Doppler shift CMB photons and broaden metal emission lines. The kSZ effect offer the most straight-forward method of measuring bulk motion within clusters, but is currently far below limits of detectability. (Sunyaev et al. 2003 [26])

### 1.1.4 Galaxies

Galaxies are massive, gravitationally bound systems, with typical sizes of  $\sim 10$  kpc and masses of  $\sim 10^{12} M_{\odot}$ . Galaxies, like our own, are made of different components; a stellar disk, bulge, stellar halo, and a dark halo. A long standing problem has been the 'flat rotation curves', obtained by measuring the circular velocities (eq. 2.12) of stars in the disk, and motions of gas clumps in the bulge. Disentangling the contributions from the different components to the total rotation curve of a galaxy shows that there has to be a halo of dark matter, with a density distribution  $\rho_{dm} \propto r^{-2}$  to account for the flat rotation curves. Typically  $\sim 50\%$  of the total mass is in the dark halo.

In the outskirts of our galaxy there are dwarf spheroidal (dSph) galaxies, which are the smallest ( $\sim 300$  pc) dark matter dominated stellar systems known in the universe. They typically contain  $\sim 400$  stars, and through dynamical analysis of the stellar motions their total masses are estimated  $\sim 10^9 M_{\odot}$  and mass-to-light ratios up to  $\Upsilon \simeq 500 (M_{\odot}/L_{\odot})$  (Gilmore et al. 2007 [6]), which means that up to 90% of their total mass is in dark matter.

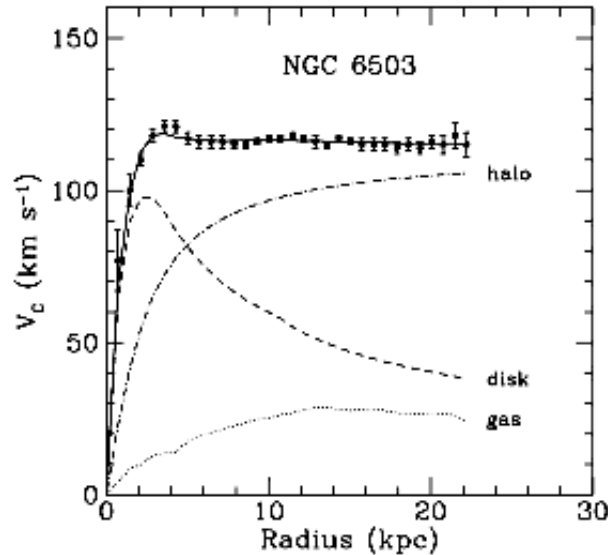


**Figure 1.3.** The measured flat rotation curve (solid line) of NGC 6503, can be explained by different contributions from the luminous disk, bulge and a dark halo (dashed lines). (Sofue & Rubin, 2001)

## 1.2 Dark matter on all scales

In this brief introduction, we have seen evidence of dark matter from the full universe, over clusters and galaxies, down to the tiny dwarf spheroidal galaxies – spanning many orders of magnitude in structure size. We have also seen that many different observational methods provide a consistent picture of the properties and the amount of dark matter.

# Chapter 2

## Theory

In this chapter we will acquire some tools that are useful when describing the dynamics of galaxy clusters.

We will introduce the fundamental equations, such as the Euler equations and the Jeans equations, which relate the gas and dark matter dynamics to their gravitational potential. We will also describe some parametric models that we will use in our further analysis.

### 2.1 Fluid mechanics

Galaxy clusters contain a hot, ionized gas fluid - the Intracluster Medium (ICM). Some of the fundamental equations from Fluid mechanics enable us to relate X-ray observed quantities like gas density and temperature to the gravitational, dynamical and thermal pressure forces.

#### 2.1.1 Continuity equation

The equation of continuity is a mass conservation equation, stating that the total mass of the fluid is constant.

$$\frac{\partial \rho}{\partial t} + \nabla \cdot (\rho \vec{v}) = 0 \quad (2.1)$$

#### 2.1.2 Euler's equation

Newton's law tells us how the velocity of a fluid element changes because of the forces. The force  $F$  per unit volume acting on the fluid is (Landau&Lifshitz, 1959 [14])

$$F = \rho \times (\text{acceleration}) = -\nabla P - \rho \nabla \Phi + F_{visc} + F_{magn} \quad (2.2)$$

The first term is the pressure force per unit volume and the second term is the external potential force per unit volume. The third and fourth term are due to the fact that a fluid can have internal friction (viscosity) or be conducting and thus be

subject to magnetic forces. We will ignore these last two terms for a while, and go on describing an ideal fluid.

The acceleration is not just  $\partial\vec{v}/\partial t$ , which is the rate at which the velocity changes at a fixed point in space - we need to know how the velocity changes for a particular piece of fluid as it moves about in space.

$$\frac{d\vec{v}}{dr} = \frac{\partial\vec{v}}{\partial t} + v_x \frac{\partial\vec{v}}{\partial x} + v_y \frac{\partial\vec{v}}{\partial y} + v_z \frac{\partial\vec{v}}{\partial z} = \frac{\partial\vec{v}}{\partial t} + (\vec{v} \cdot \nabla) \vec{v} \quad (2.3)$$

Now, we can put together Euler's equation, which is a statement of momentum conservation for an ideal fluid.

$$\rho \frac{\partial\vec{v}}{\partial t} + \rho (\vec{v} \cdot \nabla) \vec{v} = -\nabla P - \rho \nabla \Phi \quad (2.4)$$

In spherical coordinates, the radial component of eq. 2.4 looks like

$$\frac{\partial v_r}{\partial t} + v_r \frac{\partial v_r}{\partial r} + \frac{v_\theta}{r} \frac{\partial v_r}{\partial \theta} + \frac{v_\phi}{r \sin \theta} \frac{\partial v_r}{\partial \phi} - \frac{v_\theta^2 + v_\phi^2}{r} = -\frac{1}{\rho} \frac{\partial P}{\partial r} - \frac{\partial \Phi}{\partial r} \quad (2.5)$$

In the case of hydrostatic equilibrium (HSE),  $\vec{v} = 0$ , eq. 2.4 simplifies to

$$\nabla \Phi = -\frac{1}{\rho} \nabla P \quad (2.6)$$

The hydrostatic Euler equation plays a major role when estimating cluster masses from X-ray observations, by relating the total gravitational potential (l.h.s of eq. 2.6) to the density and pressure of the ICM (r.h.s of eq. 2.6). In chapter 3.4 we will allow a departure from hydrostatic equilibrium, to measure the velocities inside the cluster.

## 2.2 Jeans equations for spherical systems

There is a fundamental difference between how gas molecules in a box move about, and how galaxies in a cluster (or stars in a galaxy, or dark matter particles in a box) move about. Gas molecules are collisional, while cluster galaxies, stars in a galaxy and dark matter particles are collisionless.

The Jeans equations are derived by considering a system of identical, collisionless particles in six-dimensional phase-space  $d^6\mathbf{w}$ , where each point in phase-space is described by  $\mathbf{w} = (\mathbf{x}, \mathbf{v})$ . For the distribution function of particles in phase-space  $f(\mathbf{w}, t)$ , under a smooth potential  $\Phi(\mathbf{x}, t)$ , the collisionless Boltzmann equation is the fundamental equation for the time evolution of the system

$$\frac{df}{dt} = \frac{\partial f}{\partial t} + \sum_{\alpha=1}^6 \dot{w}_\alpha \frac{\partial f}{\partial w_\alpha} = 0 \quad (2.7)$$

### 2.3. SPHERICAL SYSTEMS

where  $\dot{\mathbf{w}} = (\dot{\mathbf{x}}, \dot{\mathbf{v}}) = (\mathbf{v}, -\nabla\Phi)$ . Integrating the Boltzmann equation over velocities, for a spherical, steady-state system (where  $\langle v_r \rangle = 0$ ,  $\sigma_r^2 = \langle v_r^2 \rangle$ ,  $\partial/\partial t = 0$ ) one can write (Binney&Tremaine 1987 [1])

$$\frac{d(\nu\overline{v_r^2})}{dr} + \frac{\nu}{r} \left( 2\overline{v_r^2} - \overline{v_\theta^2} - \overline{v_\phi^2} \right) = -\nu \frac{d\Phi}{dr} \quad (2.8)$$

where  $\nu$  is number density of the collisionless particles,  $\overline{v_i^2}$  is the second moment of the  $i$ :th velocity component and  $\Phi(r)$  is the gravitational potential.

One can define the *velocity anisotropy parameter*,  $\beta$ , to be

$$\beta \equiv 1 - \frac{\overline{v_\theta^2} + \overline{v_\phi^2}}{2\overline{v_r^2}} = 1 - \frac{\sigma_\theta^2 + \sigma_\phi^2}{2\sigma_r^2} \quad (2.9)$$

For purely circular orbits,  $\sigma_r = 0$  and  $\beta = -\infty$ , whereas for purely radial orbits,  $\sigma_\theta = \sigma_\phi = 0$  and  $\beta = 1$ . For isotropic motion,  $\sigma_r = \sigma_\theta = \sigma_\phi$ , (like gas in thermal equilibrium) one must have  $\beta = 0$ .

In terms of the anisotropy parameter eq. (2.8) reads

$$\frac{d(\nu\overline{v_r^2})}{dr} + 2\frac{\beta}{r}\nu\overline{v_r^2} = -\nu \frac{d\Phi}{dr} \quad (2.10)$$

One would expect equations describing such different things as collisional fluids and collisionless systems to look equally different, but the Jeans equation (eq. 2.8) looks quite similar to the Euler equation (eq. 2.6) (if one substitute  $\nu \rightarrow \rho_{gas}$  and  $\nu\sigma_r^2 \rightarrow P_{gas}$ ). We will in fact use this similarity to connect the Jeans equation with the Euler equation, by making some well motivated assumptions.

## 2.3 Spherical systems

*Clouds are not spheres, mountains are not cones, coastlines are not circles, and bark is not smooth, nor does lightning travel in a straight line.*

*(The Fractal Geometry of Nature, by Benoit Mandelbrot)*

Clusters of galaxies are not *perfect* spheres, but in most cases it makes sense to approximate them as spherical objects. Assuming sphericity, allows us to describe their three dimensional mass, density and temperature distributions simply as radial profiles.

### 2.3.1 Spherically symmetric matter distributions

The total gravitational potential at radius  $r$  generated by an arbitrary spherically symmetric density distribution  $\rho(\mathbf{r}')$ , may be considered to be the sum of the potentials of spherical shells. By adding the contributions from shells with  $r' < r$  and with  $r' > r$  we obtain

$$\begin{aligned}\Phi(r) &= -\frac{G}{r} \int_0^r dM(r') - G \int_r^\infty \frac{dM(r')}{r'} \\ &= -4\pi G \left[ \frac{1}{r} \int_0^r r'^2 \rho(r') dr' + \int_r^\infty r' \rho(r') dr' \right]\end{aligned}\quad (2.11)$$

Two other important properties of a spherical matter distribution are the *circular velocity* and the *escape velocity*. The circular velocity is defined to be the speed of a test particle in a circular orbit at radius  $r$

$$v_c^2(r) = r |\vec{F}| = r \frac{d\Phi}{dr} = \frac{GM(r)}{r}\quad (2.12)$$

A particle at  $r$  can escape from the gravitational potential only if its kinetic energy  $\frac{1}{2}v^2$  exceeds the value of the potential energy  $\Phi(r)$

$$v_e(r) \equiv \sqrt{2|\Phi(r)|}\quad (2.13)$$

## 2.4 Analytical models

We would of course like our analysis to be non-parametrical, relying as much as possible on the actual data. But, calculating derivatives and integrals numerically can be tricky, especially when given large error bars and few data points. Following sections will briefly discuss some parametrized models that we will use in our analysis.

### 2.4.1 Dark matter density models

Numerical simulations of the clustering of dark matter particles suggests that the mass density of the dark halo can be approximated as power laws for small and large radii, with a smooth transition at intermediate radii.

$$\rho_{dm}(r) = \frac{\rho_0}{x^\alpha (1+x)^{\beta-\alpha}} \quad , x \equiv r/r_s\quad (2.14)$$

Some important cases that have been studied are

$$(\alpha, \beta) = \begin{cases} (2, 4) & \text{for a Jaffe model} \\ (1, 4) & \text{for a Hernquist model} \\ (1, 3) & \text{for a NFW model} \end{cases}\quad (2.15)$$

## 2.4. ANALYTICAL MODELS

The mass interior to radius  $r$  can be integrated as

$$M(r) = 4\pi\rho_0 r_s^3 \int_0^{r/r_s} dx \frac{x^{2-\alpha}}{(1+x)^{\beta-\alpha}} \quad (2.16)$$

For integer values of  $(\alpha, \beta)$  this integral can be evaluated to give

$$M(r) = 4\pi\rho_0 r_s^3 \times \begin{cases} \frac{r/r_s}{1+r/r_s} & \text{for a Jaffe model} \\ \frac{(r/r_s)^2}{2(1+r/r_s)^2} & \text{for a Hernquist model} \\ \ln(1+r/r_s) - \frac{r/r_s}{1+r/r_s} & \text{for a NFW model} \end{cases} \quad (2.17)$$

It is well established that dark haloes are modelled well by the NFW model (Navarro, Frenk&White 1996 [19]), although there are indications that the central slope can be shallower than  $\alpha = 1$ .

We fit our derived dark matter density profiles,  $\rho_{dm}(r)$  using the standard NFW profile, fixing  $(\alpha, \beta) = (1, 3)$ , with  $r_s$  and  $\rho_0$  being the free parameters. We also fit a generalized NFW (gNFW) model, fixing  $\beta = 3$ , letting  $(0 < \alpha < 2)$ ,  $r_s$  and  $\rho_0$  be free parameters. In a similar fashion, we fit the integrated mass NFW (MNFW) and a generalized MNFW (gMNFW) to our derived dark matter mass profiles,  $M_{dm}(r)$ , for comparison.

### 2.4.2 Gas density models

The gas density profiles of X-ray clusters of galaxies are known to be approximated by the empirical formula, the isothermal  $\beta$ -model (Cavaliere&Fusco-Femiano 1978 [3]; Rasia et al. 2004 [23])

$$\rho_{gas}(r) = \rho_{gas,0} \frac{1}{[1 + (r/r_c)^2]^{\frac{3}{2}\beta}} \quad (2.18)$$

The observed gas density in the center of relaxed clusters usually has a power law-type cusp, instead of a flat core like the traditional isothermal  $\beta$ -model. It is also observed that the X-ray brightness profile often steepens at larger radii compared to the isothermal  $\beta$ -model. Vikhlinin et al. (2006) [13] design an extended  $\beta$ -model

$$\rho_{gas}^2(r) = \rho_{gas,0}^2 \frac{(r/r_c)^{-\alpha}}{[1 + (r/r_c)^2]^{3\beta-\alpha/2}} \frac{1}{[1 + (r/r_s)^\gamma]^{\epsilon/\gamma}} \quad (2.19)$$

where the additional parameter  $\alpha$  allows for a cusp (or core if  $\alpha = 0$ ). The additional terms describe a change of slope by  $\epsilon$  at radius  $r_s$ , and the parameter  $\gamma$  controls the width of the transition region. We follow the suggestions by Vikhlinin et al. and constrain  $\gamma = 3$  and  $\epsilon < 5$ , letting all other parameters be free when fitting.

### 2.4.3 Temperature models

Vikhlinin et al. (2006) [13] also constructed an analytical expression of a 3D temperature profile to model general features of the observed projected temperature profiles. Their model consists of two terms:

$$T_{3D}(r) = T_0 \times T_{cool}(r) \times T(r) \quad (2.20)$$

The first term,  $T_{cool}(r)$ , is designed to model the temperature decline in the central region affected by radiative cooling

$$T_{cool}(r) = \frac{(r/r_{cool})^{a_{cool}} + (T_{min}/T_0)}{(1 + r/r_{cool})^{a_{cool}}} \quad (2.21)$$

The second term,  $T(r)$ , describes a temperature decline at large radii by a broken power law profile with a transition region,

$$T(r) = \frac{(r/r_t)^{-a}}{(1 + (r/r_t)^b)^{c/b}} \quad (2.22)$$

Since our innermost temperature data are usually at  $r \sim 30$  kpc, we will not include the cooling term in our fitting procedures.

### 2.4.4 Velocity anisotropy models

Numerical simulations of collisionless dark matter particles show that for galaxy clusters  $\beta$  has a nearly universal variation, increasing from  $\sim 0$  in the central regions to  $\sim 0.5$  in the outer regions (Carlberg et al. 1997[2]; Cole&Lacey 1996 [4]; Hansen&Moore 2006 [7]).

A parametrized model that fits simulations well is given by

$$\beta(r) = \beta_{inner} + \frac{(r/r_s)^2}{1 + (r/r_s)^2}(\beta_{outer} - \beta_{inner}) \quad (2.23)$$

Alternatively, Hansen & Moore (2006) [9] proposed a universal linear relation between the velocity anisotropy  $\beta$  and the logarithmic density slope  $\gamma$  for equilibrated structures,

$$\beta(r) = 0.2(\gamma - 0.8) \quad \text{where } \gamma \equiv -\frac{d \ln \rho}{d \ln r} \quad (2.24)$$

which also fits numerical data fairly well. These relations will be of great use to our analysis of the galaxy clusters later.

## 2.5. TEMPERATURE OF DARK MATTER

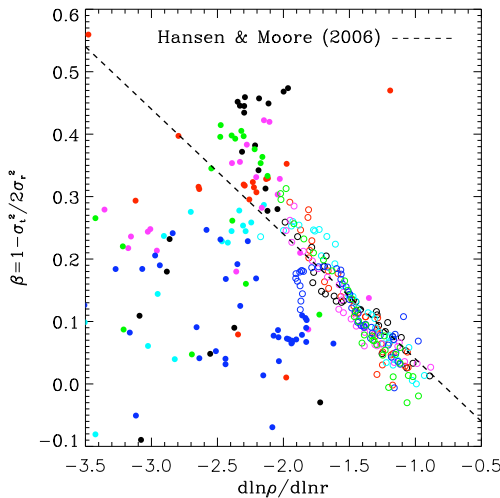


**Figure 2.1.** Local values of the logarithmic slope of the density profile ( $d\ln\rho/d\ln r$ ) plotted versus velocity anisotropy  $\beta$ . The relation proposed by Hansen & Moore (2006) [9] (dashed line) agrees well in the inner region ( $\beta \rightarrow 0$  implies motions become more isotropic), but with larger scatter for  $\gamma > 2.5$  as structures have not equilibrated fully. Considering that ( $-\infty < \beta < 1$ ), all structures land in a quite narrow band in the  $\gamma - \beta$  plane. (Navarro et al. 2008 [20])

## 2.5 Temperature of Dark matter

Despite the apparent differences between a box with collisional gas particles and an ensemble of collisionless dark matter particles, our 'substitution exercise' in the concluding section of chapter 2.2 showed that after replacing  $P_{gas} \propto \rho_{gas} T_{gas}$  with  $\rho_{dm} \sigma_{r,dm}^2$ , the Jeans and Euler equations look quite similar (with the exception of  $\beta$ ). In this section we will define an 'effective' dark matter temperature that will allow us to connect the Jeans and Euler equations.

The temperature of a baryonic gas is only well-defined when the gas is locally in thermal equilibrium, which implies energy equipartition between the gas particles achieved through collisions. Typically, the mean free paths of gas scattering are shorter than the length scales of interest in clusters ( $\sim 1$  Mpc) (Sarazin 1986 [24])

$$\lambda_e = \lambda_i \approx 23 \text{ kpc} \left( \frac{T_g}{10^8 \text{ K}} \right)^2 \left( \frac{n_e}{10^{-3} \text{ cm}^{-3}} \right)^{-1} \quad (2.25)$$

In equilibrated regions, the radial and tangential velocity dispersions of gas molecules are isotropic, which can be expressed as  $\beta_{gas} = 0$ .

Dark matter particles do not reach equilibrium through collisions, and numerical simulations of collisionless dark matter particles show that typically  $\beta_{dm} \neq 0$  (see section 2.4.4). One can define an effective dark matter 'temperature', by averaging over the three directions of the velocity dispersion

$$T_{dm} \frac{k_B}{\mu m_p} \equiv \frac{1}{3} \sigma_{dm}^2 = \frac{1}{3} (\sigma_r^2 + 2\sigma_t^2) = \sigma_r^2 \left(1 - \frac{2}{3}\beta\right) \quad (2.26)$$

Since all particle species, at a given radius, in a relaxed and spherical gravitational system have the same specific potential energy (the circular velocity of a test particle,  $v_c^2 = GM_{tot}(r)/r$  is independent of test particle mass), it is natural to assume that they also have the same average specific kinetic energy (principle of equipartition). Since the average velocity is related to the thermal energy content, one can formulate (Host et al. 2008 [11])

$$T_{dm} = \kappa(r) T_{gas} \quad (2.27)$$

The  $\kappa$ -parameter is constant, as long as the impact of radiative cooling or other non-gravitational effects are negligible. This temperature relation has been analysed in simulations by Evrard et al. (2008), and they find that

$$\kappa_{<r_{200}} \equiv \frac{k_b \overline{T_{gas}} / \mu m_p}{\sigma_{dm}^2} = 1.04 \pm 0.06 \quad (2.28)$$

Numerical simulations have convincingly shown that  $\kappa(r) = 1$  to a good accuracy (Host et al. 2008 [11]). The definition of an effective dark matter temperature (eq. 2.26) together with the temperature relation (eq. 2.27), will allow us to combine the Euler equation and the Jeans equation.

## 2.6 Considerations on the cluster dynamics

Since we have set out to measure the velocities inside clusters, it is good to get an idea of what can be expected. In this section we will review some physical processes that cause cluster motion, and results from hydrodynamical simulations of galaxy clusters.

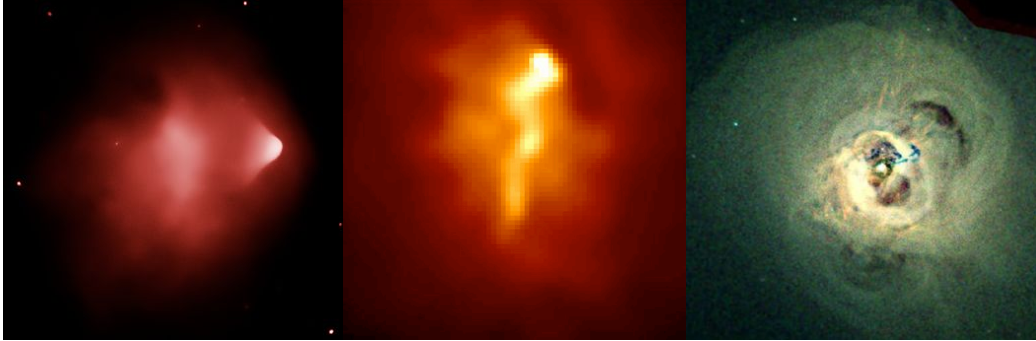


**Figure 2.2.** X-ray images displaying ongoing cluster activity. Left: Violent merger in the Bullet cluster, displaying shock fronts. Middle: Filamentary substructure of cool gas in A1795. Right: Ripples (sound waves) and cavities in the centre of the Perseus cluster, probably due to energy injection by a central black hole. In this thesis we will only analyse clusters that appear relaxed and spherical. (Credit: CHANDRA)

In 'bottom-up' hierarchical structure formation, large structures are formed at late times through subsequent merging of smaller objects. Clusters of galaxies being the most massive objects, form last (which means now) and are thus dynamically young, with typical time since last major merger  $\sim 5$  Gyr (about 20% of clusters have had more recent mergers, or are undergoing one) (Peterson&Fabian 2006 [21]).

Galaxy clusters tend to be sitting at the 'junctions' of the dark matter filaments of the cosmic web, and rather than accreting material smoothly onto a 'uniform sphere' (like in the spherical collapse model), accretion processes are expected to be lumpy, filamentary and non-spherical.

While pure dark matter simulations give insights about the non-trivial clustering of dark matter structures, inclusion of gas physics in numerical simulations increases the level of complexity further more. Hydrodynamical simulations typically include radiative cooling, (artificial) viscosity, star formation recipes, metal enrichment, magnetohydrodynamics (MHD), feedback from Active Galactic Nuclei (AGN), etc. All these physical effects are very complicated, and it is therefore hard to fully trust the gas simulations.

In following sections we will take a look at the gas velocities as seen in simulations by Fang et al. (2008) [5] and by Sunyaev, Norman&Bryan (2003) [26], to get an approximate idea of the velocity flows.

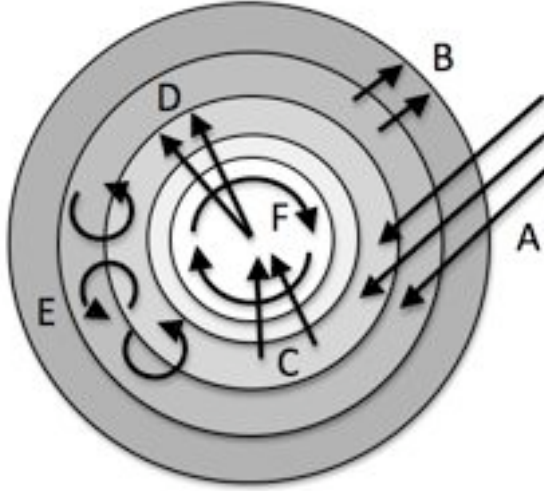


**Figure 2.3.** Schematic picture of plausible motions inside a galaxy cluster. Arrows indicate; radial in-fall at large radii (A), radial outflow at large radii (B), radial in-fall at small radii (C), radial outflow at small radii (D), turbulent/tangential motions (E) and rotational/tangential motion (F).

### 2.6.1 Radial motion

(A) & (B): Infall at large radii, due to constant bombardment of minor mergers, is very probable in hierarchical clustering. These infalling structures generate vorticity, seen as turbulent eddies (E) with sizes  $\sim 100\text{-}400$  kpc, and velocities  $v_t \sim 300\text{-}500$  km/s, throughout clusters. Lumps falling in with super-sonic velocities (sound speed in ICM  $\sim 1000$  km/s) will cause the surrounding gas to be shock-heated (Sunyaev et al. 2003).

(C) & (D): A long standing problem is the 'cooling-flow problem'. In dense cluster centers ( $r \sim$  few tens of kpc), the radiative cooling time of a plasma,  $t_{cool} \sim 5 \times 10^8$  years, always exceeds the gravitational dynamical time, which is expected to lead to a slow, subsonic inflow towards the center (making the core even denser and cool even faster) (Peterson&Fabian 2006 [21]). This effect might be compensated by energy injection from AGN, which offers an explanation to why clusters do not suffer from overcooling. Simulations of supersonic narrow jets produced by AGN, show that the hypothesised cooling flows can be heated and transported outwards (B) creating cavities in the ICM (similar to what is observed in the Perseus cluster, left panel of fig. 2.2) (Omma et al. 2003).

## 2.6. CONSIDERATIONS ON THE CLUSTER DYNAMICS

### 2.6.2 Tangential motion

(E): Simulations by Fang et al. (2008) show that infalling material can maintain small scale turbulence (eddies of size  $\sim 20\text{-}150$  kpc, with velocities  $\sim 25\text{-}60\%$  of virial velocity), which is damped by viscous heating.

(F): Ordered rotational motion within the central few hundred kpc is seen in simulations by Fang et al. (2008) and Sunyaev et. al. (2003), with typical velocities  $v_t \sim 300\text{-}600$  km/s. These motions are likely induced by off-axis mergers. In the classic cooling flow model, gas rotation is also expected, due to mass and angular momentum conservation.

In conclusion, these numerical simulations show that very complicated velocity patterns may appear, and that we may expect radial variations in both the tangential and radial velocity components.

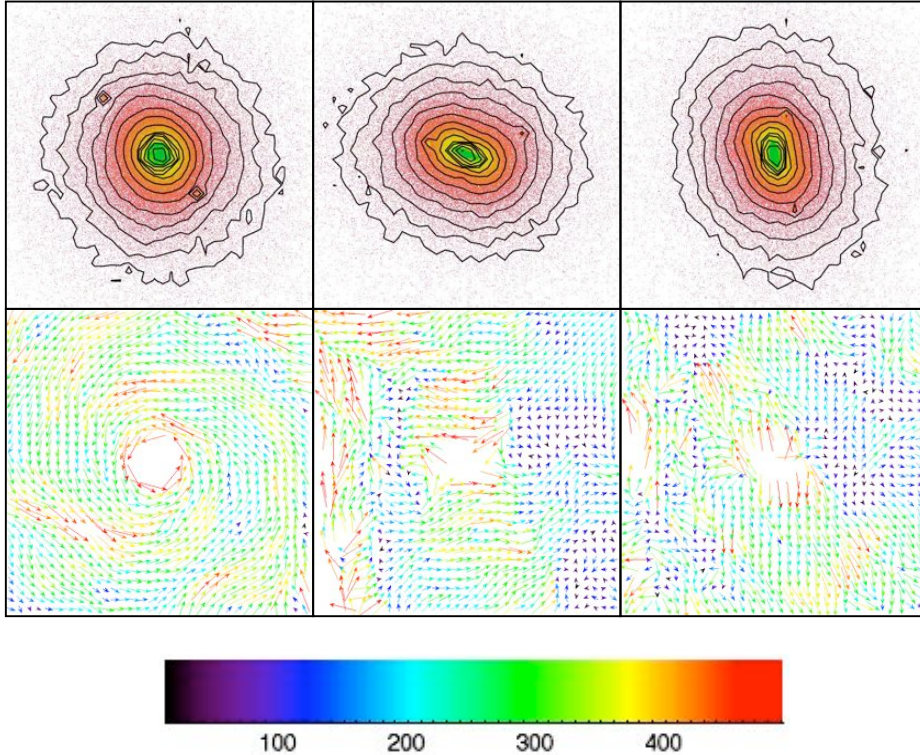


**Figure 2.4.** Top panel: Mock X-ray flux maps of a simulated cluster from x,y and z projection. Bottom panel: slices of the velocity field in the center of the simulated cluster in the y-z, x-z and x-y planes. The bottom color bar is for the velocity field, in units of km/s. Each box has a size of  $1 \text{ h}^{-1} \times 1 \text{ h}^{-1} \text{ Mpc}^2$ . (Fang et al. 2008 [5])



## Chapter 3

# X-ray Observations of Clusters

### 3.1 Physics of the Intracluster Medium

Clusters have total masses of about  $10^{14}$  to  $10^{15} M_{\odot}$ , with a total gas fraction of  $\sim 16\%$  (where about  $13\%$  is in the ICM and about  $3\%$  in the cluster galaxies). The remaining  $84\%$  of the mass is in dark matter.

Gas densities vary from  $\sim 10^{-3} - 10^{-1} \text{cm}^{-3}$  in cluster centres. (Peterson&Fabian 2006 [21]; Sarazin 1986 [24])

The Intracluster Medium (ICM) is a nearly fully *ionized plasma* due to the high temperatures  $\sim 10^7$ - $10^8$  K ( $\sim 1$ - $10$  keV) created by the deep gravitational potential. This means that light elements like hydrogen and helium are fully stripped of their electrons, and heavier elements retain only a few of their electrons.

When free electrons are accelerated in the coulomb field of an ion, huge amounts of thermal bremsstrahlung emission are produced, making galaxy clusters among the most X-ray luminous objects known to man.

The power per energy per volume emitted through bremsstrahlung is approximately

$$\frac{d^2P}{dVdE} \approx 10^{-11} n_e n_H T_e^{-\frac{1}{2}} e^{-\frac{E}{k_B T_e}} \text{ cm}^{-3} \text{ s}^{-1} \quad (3.1)$$

where  $n_e$  is the electron density,  $n_H$  is the hydrogen density,  $E$  is the photon energy and  $T_e$  is the electron temperature. The total power per volume radiated is

$$\frac{dP}{dV} \approx 10^{-27} n_e n_H T_e^{\frac{1}{2}} \text{ ergs cm}^{-3} \text{ s}^{-1} \quad (3.2)$$

Due to the low ICM densities, the plasma can be treated as optically-thin, which means that radiation almost completely escapes without interaction with the plasma. This allows us to measure quantities like gas density and temperature at various positions in the cluster, through X-ray spectroscopy and imaging.

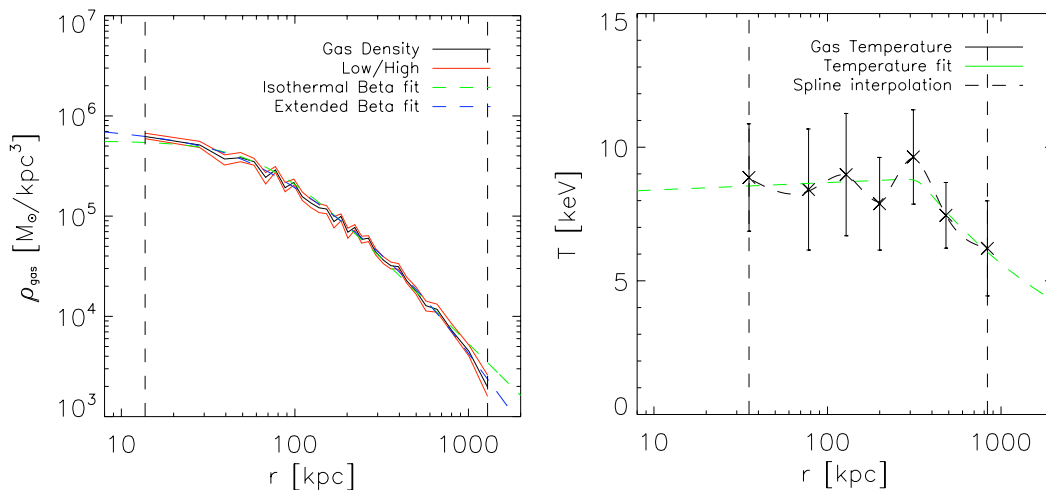


**Figure 3.1.** Left: Deprojected observed radial profile of gas density (solid black line) within  $1\sigma$  error (red solid lines) of A1689. The extended  $\beta$ -model (eq. 2.19) offers a better fit (dashed blue line) than the cored isothermal  $\beta$ -model (green dashed line). Right: Deprojected observed radial profile of gas temperature (black crosses) and corresponding  $1\sigma$  error bars of A1689. The green dashed line shows the temperature fitted by eq. 2.20 and the black dashed line is a 3-point spline interpolation. Vertical lines mark the innermost and outermost radii of observations.

## 3.2 X-ray analysis

X-ray observations provide us with two-dimensional projected gas density and temperature of the ICM. These can be de-projected (see Morandi et. al (2007)[17] or appendix A for a simpler method) to deduce the three-dimensional radial profiles of gas density,  $\rho_g(r)$ , and gas temperature,  $T_g(r)$ .

For relaxed and spherically symmetric galaxy clusters, one can use the Euler equation (eq. 2.4) to relate the total mass of gravitating matter at a given radius to the radial dependence of gas temperature and density. This is usually done under the assumption of hydrostatic equilibrium (eq. 2.6),

$$\frac{GM_{\text{tot}}(r)}{r^2} = -\frac{1}{\rho_g} \frac{\partial P_g}{\partial r} \quad (3.3)$$

### 3.2. X-RAY ANALYSIS

where  $\rho_g(r)$  is the gas density and  $P_g(r)$  is the gas pressure.

It is assumed that the total gas pressure is represented by the thermal pressure,

$$P_g = P_{thermal} = n_e k_B T_g = \frac{\rho_g k_B T_g}{\mu m_p} \quad (3.4)$$

where  $m_p$  is the proton mass,  $\mu m_p$  is the mean mass per particle (we adopt  $\mu = 0.61$ ). Combining eq. 3.3 and eq. 3.4 allows us to write

$$v_c^2(r) = \frac{GM_{tot}(< r)}{r} = -\frac{k_B T_g}{\mu m_p} \left( \frac{d \ln \rho_g}{d \ln r} + \frac{d \ln T_g}{d \ln r} \right) \quad (3.5)$$

Throughout the analysis, all uncertainties are calculated using a Monte Carlo technique, whereby the deprojected gas temperature and density data are perturbed 10000 times assuming Gaussian uncertainties.

To obtain the total mass profile  $M_{tot}(r)$ , we calculate the logarithmic derivatives in eq. 3.5 using 3-point Lagrangian interpolation (with linear interpolation for the endpoints). The result is shown in left panel of fig. 3.2.

Most analyses have required the derived total mass profile  $M_{tot}(r)$  to be monotonically increasing, since otherwise you would end up with an 'unphysical' negative density. In our analysis, we do not want to restrict our selves to that assumption, because a dip in the reconstructed mass profile indicates loss of hydrostatic equilibrium. Ignoring velocity terms in the full Euler equation (eq. 2.4) can lead both to over- and underestimation of the hydrostatic (HS) reconstructed mass. Remember; these are the velocities that we want to measure.

From the total mass profile,  $M_{tot}(r)$ , we can obtain  $\rho_{tot}(r)$  in two ways

$$\rho_{tot}(r) = \begin{cases} \frac{\Delta M_{tot}}{\Delta V_{shell}} & \text{(a)} \\ \frac{1}{4\pi r^2} \frac{dM_{tot}}{dr} & \text{(b)} \end{cases} \quad (3.6)$$

The intuitive approach (eq. 3.6.a), is to calculate  $\rho_{tot}(r)$  simply as the total mass inside the  $i$ :th spherical shell,  $\Delta M_{tot,i} = (M_{bin,i+1} - M_{bin,i})$ , divided by the volume of shell  $i$ ,  $\Delta V_{shell} = \frac{4\pi}{3}(r_{bin,i+1}^3 - r_{bin,i}^3)$ . We use linear interpolation to calculate the total mass at the bin edges.

One can also obtain  $\rho_{tot}(r)$  by numerical differentiation of  $M_{tot}(r)$  (eq. 3.6.b), using a 3-point Lagrangian interpolation (with linear interpolation for the endpoints). It is helpful to restrict  $M_{tot}(r=0) = 0$ . Both methods perform equally well, with the numerical differentiation-method yielding slightly smaller error bars.

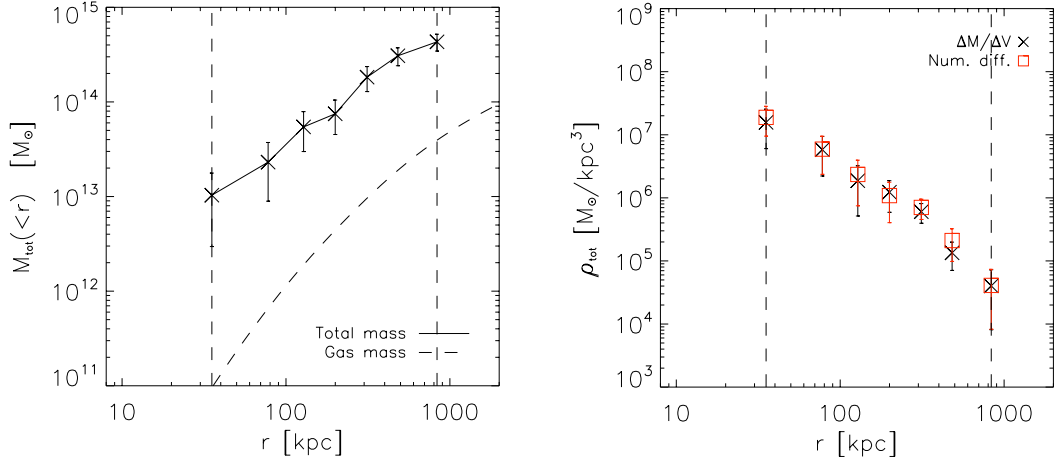


**Figure 3.2.** Hydrostatic (HS) analysis of A1689. Left: Total mass profile,  $M_{tot}(r)$ , calculated assuming hydrostatic equilibrium (eq. 3.5) (black line with crosses) with  $1\sigma$  errorbars. Gas mass profile (black dashed line) shown for comparison. Right: Total mass density obtained using eq. 3.6.a (black crosses) and eq. 3.6.b (red squares) and corresponding  $1\sigma$  errorbars.

The dark matter mass and density profiles are now easily obtained either by  $M_{dm}(r) = M_{tot}(r) - 4\pi \int \rho_g(r)r^2 dr$  or by  $\rho_{dm} = \rho_{tot} - \rho_g$ .

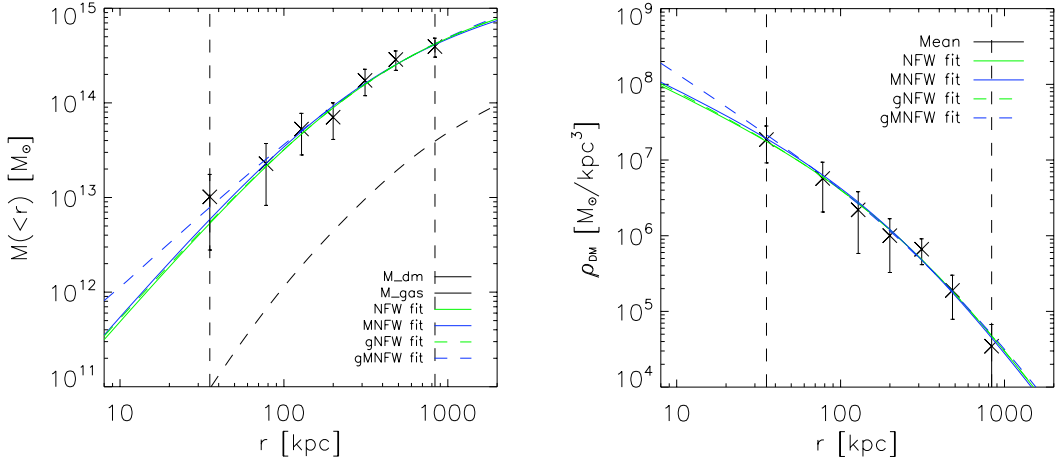


**Figure 3.3.** Hydrostatic (HS) analysis of A1689. Left: Dark matter mass profile  $M_{dm}(r)$  (black crosses) with  $1\sigma$  uncertainties. Gas mass profile (black dashed line) shown for comparison. Right: Dark matter density profile  $\rho_{dm}$  (black crosses) with  $1\sigma$  uncertainties. Solid green and blue lines show fitted NFW and gNFW models.

### 3.3. CALCULATING THE RADIAL VELOCITY DISPERSION

As seen in fig. 3.3, the NFW model fits the calculated dark matter density well. The only exception in this specific case, is the generalized integrated mass NFW model (gMNF<sub>W</sub>, blue dashed line) with fitted inner slope  $\alpha = 1.4$ .

## 3.3 Calculating the radial velocity dispersion

To make the connection with the dark matter, we must consider the Jeans equation (Binney&Tremaine, 1987 [1]), which relates the dark matter density and velocity dispersions with the total gravitating mass;

$$v_c^2(r) = \frac{GM_{tot}(< r)}{r} = -\sigma_r^2 \left( \frac{d \ln \rho_{dm}}{d \ln r} + \frac{d \ln \sigma_r^2}{d \ln r} + 2\beta \right) \quad (3.7)$$

The total mass  $M_{tot}(r)$  is obtained from the hydrostatic Euler equation, the dark matter density is easily obtained through  $\rho_{dm} = \rho_{tot} - \rho_g$ . But, the Jeans equation is not closed, in the sense that  $\sigma_r^2$  and  $\beta$  cannot both be determined from  $M_{tot}(r)$  and  $\rho_{dm}$ . In the following sections we will step by step see how to get around this by making some further assumptions.

#### 3.3.1 $\beta = \text{constant}$

The most direct approach to calculate the radial velocity dispersion is to regard the Jeans equation (eq. 3.7) as a first-order differential equation for  $\rho_{dm}\sigma_r^2$ , assuming a constant value or a functional form for  $\beta$ .

In the case  $\beta = \text{constant}$ , one finds the integrating factor to be  $e^{\int dr\beta/r} = r^{2\beta}$ , so the solution can be written in closed form. The solution that satisfies the boundary condition  $\lim_{r \rightarrow \infty} v_r^2 = 0$  is

$$\sigma_r^2(r) = \frac{1}{r^{2\beta}\rho_{dm}(r)} \int_r^\infty r'^{2\beta} \rho_{dm}(r') \frac{GM(< r')}{r'^2} dr' \quad (3.8)$$

Hansen&Piffaretti (2007) [8] do a completely non-parametric analysis of two relaxed clusters. By calculating  $\sigma_r^2$  as in eq. 3.8, using constant values of  $\beta \sim 0.3 - 0.6$  (which are in good agreement with numerical simulations), they show that the reconstructed dark matter temperature  $T_{dm}$  (defined in eq. 2.26) is in good agreement with the gas temperature in the outer regions of the clusters. This supports that the temperature relation  $T_{dm} = \kappa T_g$  (discussed in section 2.5) is indeed valid.

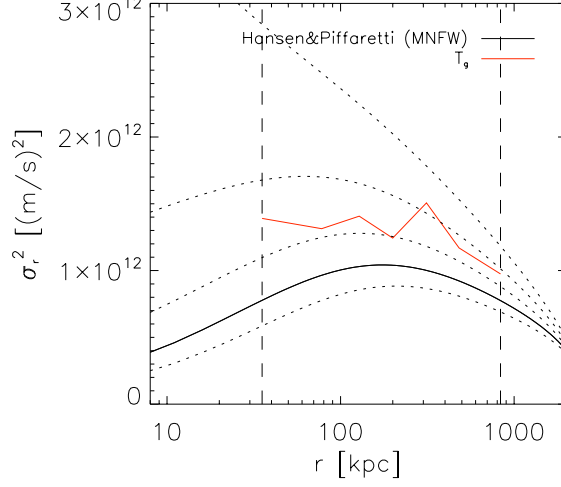


**Figure 3.4.** Dark matter radial velocity dispersion  $\sigma_r^2$ , calculated using eq. 3.8 for constant values of  $\beta = 0$  (black solid line) and  $\beta = -0.2, 0.2, 0.4, 0.6$  (dotted black lines) using a fitted NFW profile. Shown for comparison is the scaled gas temperature,  $k_B T_g / \mu m_p$  (red line). This indicates that  $\beta$  is indeed non-zero, in agreement with numerical simulations.

### 3.3.2 $\beta = \beta(r)$

Host et al. (2008) [11] present a method to calculate both the radial velocity dispersion and the velocity anisotropy, based on the definition of dark matter temperature (eq. 2.26) and the temperature relation (eq. 2.27)

$$T_{dm} = \kappa T_g \Rightarrow 2\beta\sigma_r^2 = 3\sigma_r^2 - 3\kappa \frac{k_B T_g}{\mu m_p} \quad (3.9)$$

By equating the hydrostatic Euler equation (eq. 3.5) and the Jeans equation (eq. 3.7),  $\beta(r)$  can be eliminated using eq. (3.9)

$$\sigma_r^2 \left( \frac{d \ln \rho_{dm}}{d \ln r} + \frac{d \ln \sigma_r^2}{d \ln r} + 3 \right) = \frac{k_B T_g}{\mu m_p} \left( \frac{d \ln \rho_g}{d \ln r} + \frac{d \ln T_g}{d \ln r} + 3\kappa \right) \quad (3.10)$$

After finding the integrating factor, we can calculate the radial velocity dispersion using only observables:

$$\sigma_r^2(r) = \frac{1}{\rho_{dm}(r)r^3} \int_0^r \rho_{dm}(r')r'^2 \left( \frac{3\kappa k_B T_g}{\mu m_p} - \frac{GM(< r')}{r'} \right) dr' \quad (3.11)$$

Now,  $\beta(r)$  can be recovered in two ways - either through the Temperature relation (TR) or the Jeans equation (JE)

$$\beta_{TR}(r) = \frac{3}{2} \left( 1 - \kappa \frac{k_B T_g}{\mu m_p \sigma_r^2} \right) \quad (3.12)$$

### 3.4. INFERRING THE VELOCITY COMPONENT

$$\beta_{JE}(r) = -\frac{1}{2} \left( \frac{d \ln \rho_{dm} \sigma_r^2}{d \ln r} + \frac{GM_{tot}}{r \sigma_r^2} \right) \quad (3.13)$$

Performing this analysis, we recover the radial variation of  $\beta$  using both methods. The result is shown in fig. 3.5) and we find excellent agreement with Host et al. (2008).

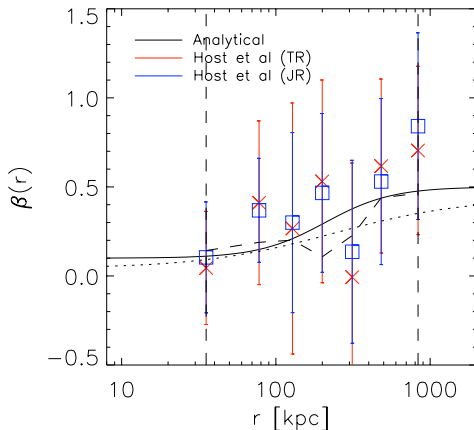


**Figure 3.5.** Inferred velocity anisotropy parameter, recovered using the Temperature Relation (eq. 3.12) (red crosses), or using the Jeans Relation (eq. 3.13). Shown is also the analytical model for  $\beta(r)$  (eq. 2.23) (solid black line) and the  $\beta$ - $\gamma$ -relation (Hansen&Moore, 2006) (eq. 2.24) using calculated dark matter density (dashed black line) or a fitted NFW profile (dotted black line)

## 3.4 Inferring the velocity component

We have so far assumed that gas velocities can be ignored, in order to use the traditional hydrostatic equilibrium. We will now allow for the velocity terms that appear in the Euler equation (eq. 2.4) to be non-zero. After ignoring terms that include the time derivative  $\partial/\partial t$  and angular derivatives  $\partial/\partial\theta$ ,  $\partial/\partial\phi$  of  $v_r$ , we can write

$$v_r \frac{\partial v_r}{\partial r} - \frac{v_t^2}{r} = -\frac{1}{\rho} \frac{\partial}{\partial r} \left( \frac{\rho_g k_B T_g}{\mu m_p} \right) - \frac{GM_{tot}}{r^2} \quad (3.14)$$

To make the connection with the Jeans equation, we will use the temperature relation,  $T_{dm} = \kappa T_g$ , and an analytical expression for the velocity anisotropy parameter,  $\beta(r)$ , that varies from  $\sim 0.1$  at small radii to  $\sim 0.5$  at large radii. As discussed in section 2.5 and 2.4.4, both these assumptions are in excellent agreement with numerical simulations.

The radial velocity dispersion is then completely determined,  $\sigma_r^2 = \sigma_r^2(\kappa, T_g, \beta)$ ,

$$\sigma_r^2(r) = \frac{k_B}{\mu m_p} T_{dm}(r) \frac{1}{1 - \frac{2}{3}\beta(r)} \equiv \frac{k_B}{\mu m_p} \kappa(r) T_g(r) f_\beta(r) \quad (3.15)$$

Combining the Euler equation (eq. 3.14) with the Jeans equation (eq. 3.7) leaves us with

$$\begin{aligned} r v_r \frac{\partial v_r}{\partial r} - v_t^2 &= \sigma_r^2 \left( \frac{d \ln \rho_{dm}}{d \ln r} + \frac{d \ln \sigma_r^2}{d \ln r} + 2\beta \right) - \frac{k_B T_g}{\mu m_p} \left( \frac{d \ln \rho_g}{d \ln r} + \frac{d \ln T_g}{d \ln r} \right) \\ &= \frac{k_B T_g}{\mu m_p} \left[ \kappa f_\beta \left( \frac{d \ln \rho_{dm}}{d \ln r} + \frac{d \ln \kappa T_g f_\beta}{d \ln r} + 2\beta \right) - \left( \frac{d \ln \rho_g}{d \ln r} + \frac{d \ln T_g}{d \ln r} \right) \right] \\ &= \frac{k_B T_g}{\mu m_p} \left[ \underbrace{\kappa f_\beta \frac{d \ln(\rho_{dm}/\rho_g)}{d \ln r}}_{\text{Term 1}} + \underbrace{(\kappa f_\beta - 1) \left( \frac{d \ln \rho_g T_g}{d \ln r} \right)}_{\text{Term 2}} + \underbrace{\kappa f_\beta \left( \frac{d \ln \kappa f_\beta}{d \ln r} + 2\beta \right)}_{\text{Term 3}} \right] \end{aligned} \quad (3.16)$$

On the left hand side of eq. 3.16 are the radial and tangential velocity terms that we are trying to measure (hereafter referred to as the 'velocity component'), which other authors assuming hydrostatic equilibrium explicitly put to zero.

The right hand side of eq. 3.16 contains X-ray observables (gas density  $\rho_g$  and temperature  $T_g$ ), the dark matter density  $\rho_{dm}$ , the  $\kappa$ -parameter and the velocity anisotropy parameter  $\beta(r)$ .

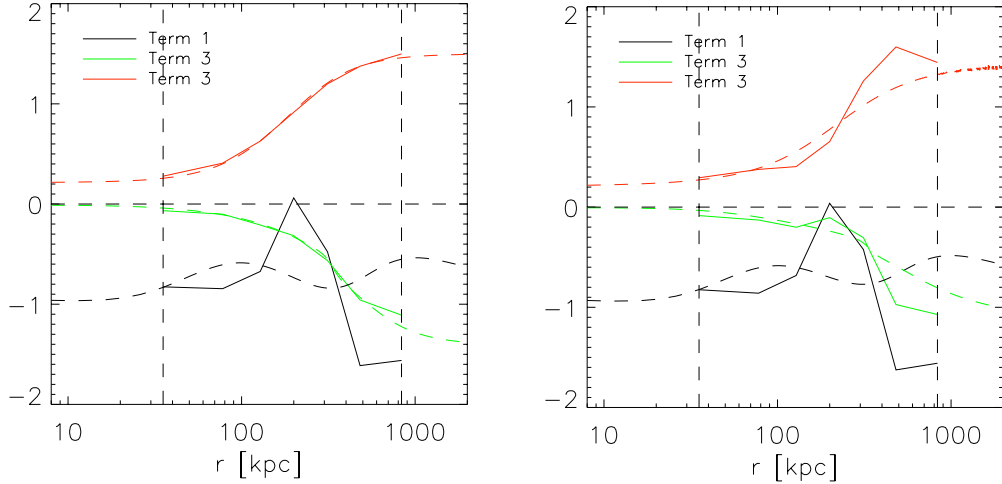


**Figure 3.6.** Both panels show the r.h.s of eq. 3.16 divided into terms 1,2 and 3. The solid lines show the radial behaviour of the different terms, based on observed  $\rho_g(r), T_g(r)$ , calculated  $\rho_{dm}(r)$  and assumed  $\beta(r)$ . Dashed lines show the behaviour of the corresponding fitted profiles. Left:  $\beta(r)$  is the analytical model described in eq. 2.23. Right:  $\beta(r)$  is described through the Hansen&Moore-relation (eq. 2.24)

### 3.4. INFERRING THE VELOCITY COMPONENT

Dividing the r.h.s of eq. 3.16 into three terms lets us study it in greater detail.

The first term (black lines in fig. 3.6) includes the logarithmic derivative of the fraction of dark matter and gas density,  $\rho_{dm}/\rho_g$ . We use the dark matter density obtained through the ordinary hydrostatic analysis as a first approximation. Due to small local fluctuations in the derived dark matter density, and the fact that we are restricted to relatively few data points, even larger fluctuations are induced when calculating the derivative.

The second term (green lines in fig. 3.6) is again the hydrostatic Euler equation, but here multiplied by the factor  $(\kappa f_\beta - 1)$ .

The third term (red lines in fig. 3.6) arises only from the assumed  $\kappa = 1$  and  $\beta(r)$ . The left panel of fig. 3.6 shows the analysis made using the analytical model in eq. 2.23 with  $\beta_{inner} = 0.1$  and  $\beta_{outer} = 0.5$ . This is to compare with the right panel of fig. 3.6, where  $\beta(r)$  is determined through the  $\beta - \gamma$ -relation in eq. 2.24.

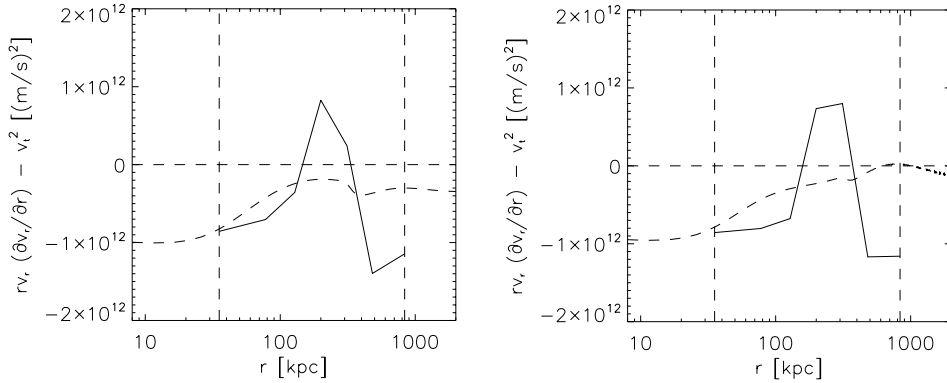


**Figure 3.7.** Velocity component (l.h.s of eq. 3.16) of A1689. Black solid lines show the inferred velocity component calculated without use of any parametric models. Dashed lines show the inferred velocity component using only fitted profiles. Performing the analysis with  $\beta(r)$  defined as in eq. 2.23 (left panel) yields slightly different velocities than with  $\beta(r)$  defined through eq. 2.24 (right panel).

#### 3.4.1 Tangential motion

The velocity component (l.h.s of eq. 3.16) consists of two terms, one tangential and one radial. We first consider the tangential.

If contributions come only from the tangential velocity term ( $-v_t^2$ ), the negative deviations in fig. 3.7 would correspond to tangential velocities  $v_t$  up to  $\sim 800$  km/s.

In some sense, the tangential velocity term, acts like a proper 'non-thermal pressure' because of the minus-sign and the square. Neglecting such velocities in the hydrostatic analysis means the reconstructed mass is *underestimated*.

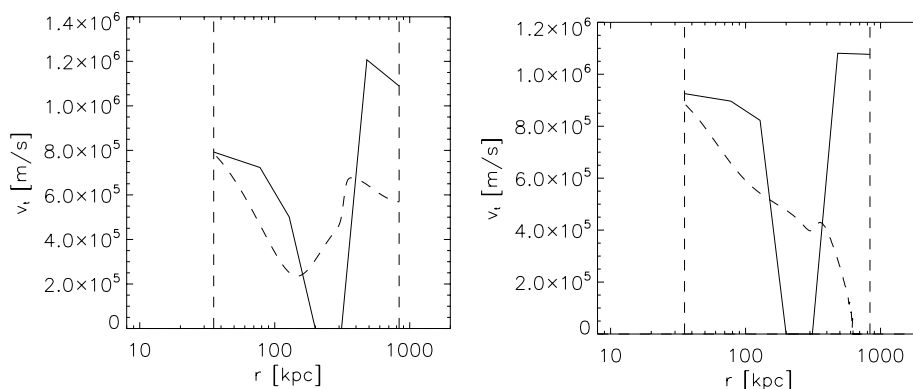


**Figure 3.8.** Considering only tangential motion for A1689. Inferred tangential velocities from non-parametric analysis (solid lines), and from parametric analysis (dashed lines). Left:  $\beta(r)$  from eq. 2.23 Right:  $\beta(r)$  from eq. 2.24.

### 3.4.2 Radial motion

The radial velocity term ( $rv_r \frac{\partial v_r}{\partial r}$ ) also contributes to deviations in fig. 3.7, given that  $\partial v_r / \partial r$  is sufficiently large.

Interestingly, due to the possibility of  $v_r$  and  $\partial v_r / \partial r$  having different signs, radial motion could contribute to both negative and/or positive deviations in fig. 3.7.

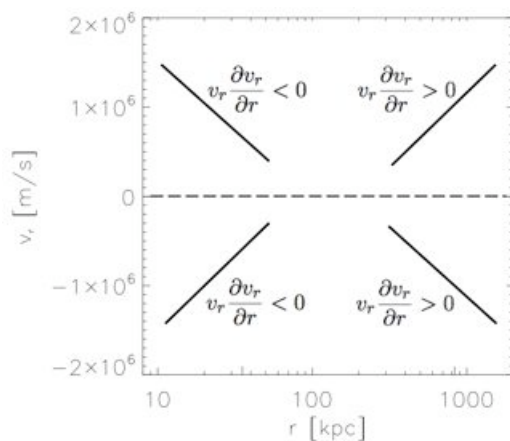


**Figure 3.9.** The radial velocity term can make both negative and positive contributions to the velocity component. Because of the 'sign degeneracy' it is not possible to distinguish between infall ( $v_r < 0$ ) and outflow ( $v_r > 0$ ).

Both decelerating outflow and accelerating infall would make negative contributions in fig. 3.7, similar to the tangential velocity component.

### 3.5. CONCLUSION AND FUTURE IMPROVEMENTS

The only way of getting a positive deviation in fig. 3.7, is either through decelerating infall or accelerating outflow. Radial motion could in that case act like a negative 'non-thermal pressure'! If such radial motions are neglected in the hydrostatic analysis, the reconstructed mass would be *overestimated*.

Unfortunately, because of the 'sign degeneracy', there is no way to distinguish between accelerating infall or decelerating outflow (or between decelerating infall and accelerating outflow either), which of course is a weak point. Bearing this in mind, one can still attempt to solve

$$v_r \frac{\partial v_r}{\partial r} = \frac{f(r)}{r} \Rightarrow \int v_r dv_r = \frac{v_r^2}{2} + C = \int \frac{f(r)}{r} dr \quad (3.17)$$

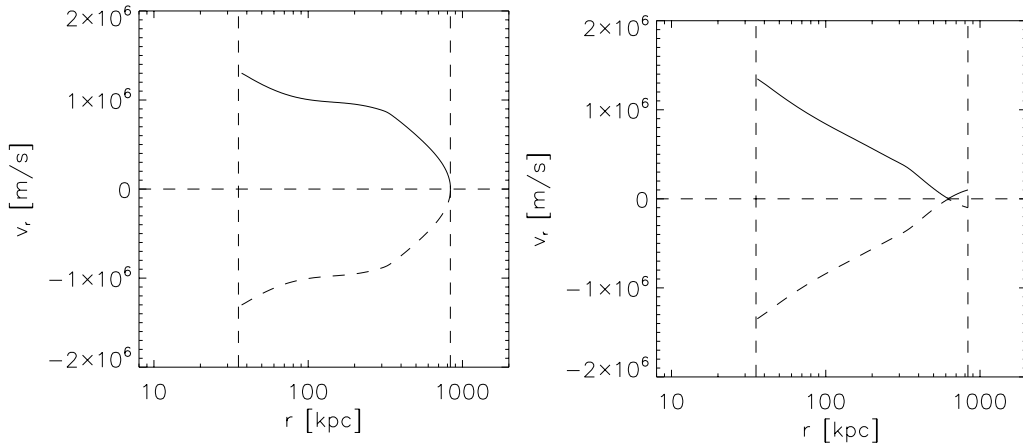


**Figure 3.10.** The case with radial motion only for A1689. The inferred radial velocities are calculated through eq. 3.17 using the fitted profiles. Because of the 'sign degeneracy' there is no way to distinguish between radial infall (dashed line) or outflow (solid line). Left:  $\beta(r)$  from eq. 2.23 Right:  $\beta(r)$  from eq. 2.24.

### 3.5 Conclusion and future improvements

We have attempted to derive the velocities inside clusters, using only X-ray observations – something that has not been considered before. We did this by connecting the Euler equation with the Jeans equation, through some well considered assumptions on the velocity anisotropy  $\beta(r)$  and on the temperature of the dark matter.

We find tentative indication that there is significant gas motion in the galaxy cluster, with velocities up to  $\sim 500$ - $1000$  km/s. These velocities are most likely unreasonably large (numerical simulations usually indicate velocities of the order few hundred km/s).

### CHAPTER 3. X-RAY OBSERVATIONS OF CLUSTERS

One important future improvement of the present analysis is to make it iterative. The problem is that the dark matter density profile is found under the assumption of hydrostatic equilibrium (zero velocity). One should take the inferred velocities and include them in the full Euler equation, while analysing the dark matter mass profile. Our first primitive attempts to do this (not described in the thesis) did not converge.

## Appendix A

# Geometrical Deprojection



Figure A.1. 2D Projection of a 3D balloon

One can perform a non-parametric deprojection of the observed 2D density and temperature profiles, with an 'onion peeling' approach, similar to McLaughlin (1999) [16], under the assumption of spherical symmetry.

The projected density and temperature,  $\rho_i^{2D}$  and  $T_i^{2D}$ , are observed in  $N$  concentric annular regions on the sky, where  $R_i$  and  $R_{i+1}$  are the inner and outer radii of the  $i$ :th annulus.

The volume common to a spherical shell,  $r_i \leq r \leq r_{i+1}$ , and a cylindrical ring,  $R_i \leq R \leq R_{i+1}$ , is

$$V_{ij} = \begin{cases} \frac{4\pi}{3} \left[ \left( r_{i+1}^2 - R_j^2 \right)^{\frac{3}{2}} - \left( r_{i+1}^2 - R_{j+1}^2 \right)^{\frac{3}{2}} - \left( r_i^2 - R_j^2 \right)^{\frac{3}{2}} + \left( r_i^2 - R_{j+1}^2 \right)^{\frac{3}{2}} \right] & (i \geq j) \\ 0 & (i < j) \end{cases} \quad (\text{A.1})$$

Any term in parentheses that evaluates as negative is set to zero. An obvious choice of shell radii is,  $r_i = R_i$ .

## APPENDIX A. GEOMETRICAL DEPROJECTION

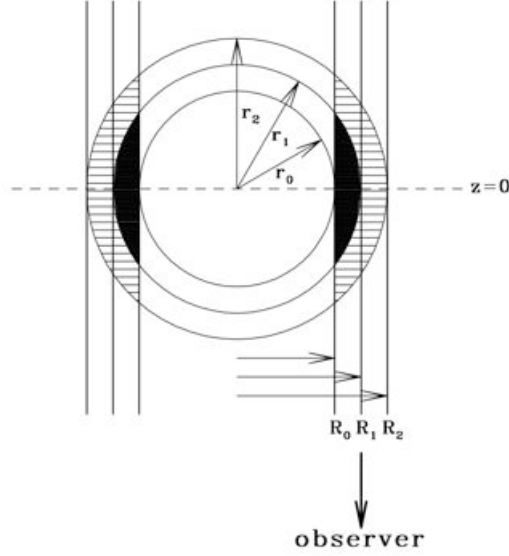


**Figure A.2.** Illustration of geometrical deprojection algorithm. Radii  $r_0, r_1, r_2$  are three-dimensional quantities, and define spherical shells. Radii  $R_0, R_1, R_2$  are projected quantities referring to cylindrical shells aligned along the line of sight (McLaughlin 1999 [16]).

To deproject the density, one can simply assume that the density of the outermost shell equals that of the outermost annulus,  $\rho_N^{3D} = \rho_N^{2D}$  (hoping that the X-ray emission is negligible outside of the outermost annulus). Then, density of shell  $i = N - 1$  can be calculated, and one can proceed in an iterative manner, from the outside in ("peeling the onion").

$$\rho_i^{3D} V_{i,i} = \rho_i^{2D} \frac{4\pi}{3} \left[ \left( r_N^2 - R_i^2 \right)^{\frac{3}{2}} - \left( r_N^2 - R_{i+1}^2 \right)^{\frac{3}{2}} \right] - \sum_{j=i+1}^N \rho_j^{3D} V_{j,i} \quad (\text{A.2})$$

The observed projected temperature  $T_i^{2D}$  from annulus  $R_i \leq R \leq R_{i+1}$  can be regarded as a superposition of the temperature of shell  $i$  and contributions from obscuring shells, weighted by  $w_{i,j} = (\rho_j^{3D})^2 V_{i,j}$ . Again we assume  $T_N^{3D} = T_N^{2D}$ , and proceed peeling inwards.

$$w_{i,i} T_i^{3D} = T_i^{2D} \sum_{j=i+1}^N w_{i,j} - \sum_{j=i+1}^N w_{i,j} T_j^{3D} \quad (\text{A.3})$$

## Appendix B

# Navier-Stokes equation

The Navier-Stokes equation enforces momentum conservation for a fluid with internal friction (viscosity). This equation relates the momentum of the fluid (left hand side) to the gravitational compression (first term on the right hand side), the thermal pressure gradients, and viscous forces (last terms). In Cartesian coordinates it can be written as

$$\rho \left( \frac{\partial v_i}{\partial t} + v_j \frac{\partial v_i}{\partial x_j} \right) + \rho \frac{\partial \Phi}{\partial x_i} = -\frac{\partial P}{\partial x_i} + \frac{\partial}{\partial x_j} \eta \left( \frac{\partial v_i}{\partial x_j} + \frac{\partial v_j}{\partial x_i} - \frac{2}{3} \delta_{ij} \frac{\partial v_k}{\partial x_k} \right) + \frac{\partial}{\partial x_i} \left( \zeta \frac{\partial v_k}{\partial x_k} \right) \quad (\text{B.1})$$

where  $\eta > 0$  and  $\zeta > 0$  are the first and second coefficients of viscosity. In spherical coordinates, and  $\nu = \eta/\rho$ , the radial part of eq. B.1 reads

$$\frac{\partial v_r}{\partial t} + v_r \frac{\partial v_r}{\partial r} + \frac{v_\theta}{r} \frac{\partial v_r}{\partial \theta} + \frac{v_\phi}{r \sin \theta} \frac{\partial v_r}{\partial \phi} - \frac{v_\theta^2 + v_\phi^2}{r} + \frac{\partial \Phi}{\partial r} = -\frac{1}{\rho} \frac{\partial P}{\partial r} + \nu \left[ \frac{1}{r^2} \frac{\partial}{\partial r} \left( r^2 \frac{\partial v_r}{\partial r} \right) + \frac{1}{r^2 \sin \theta} \frac{\partial}{\partial \theta} \left( \sin \theta \frac{\partial v_r}{\partial \theta} \right) + \frac{1}{r^2 \sin^2 \theta} \frac{\partial^2 v_r}{\partial \phi^2} \right] \quad (\text{B.2})$$

We will neglect the additional terms introduced in the Navier-Stokes equation in our analysis, since the second derivatives of the radial velocity and the viscosity coefficient of the hot, low density plasma are likely to be very small (Sarazin 1986 [24]).



## Appendix C

# Selection of analysed clusters

### C.1 RXJ1347.5

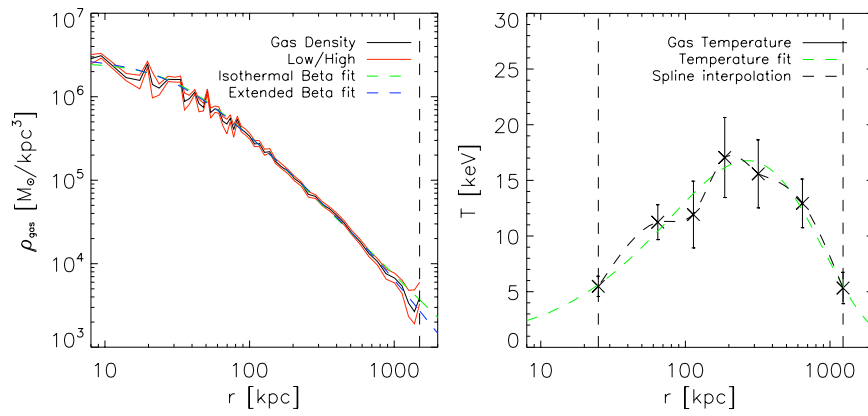
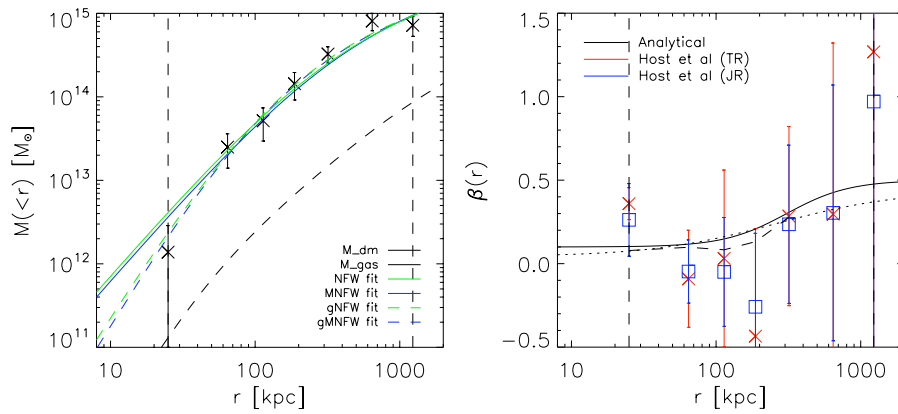


Figure C.1.



APPENDIX C. SELECTION OF ANALYSED CLUSTERS

Figure C.2.

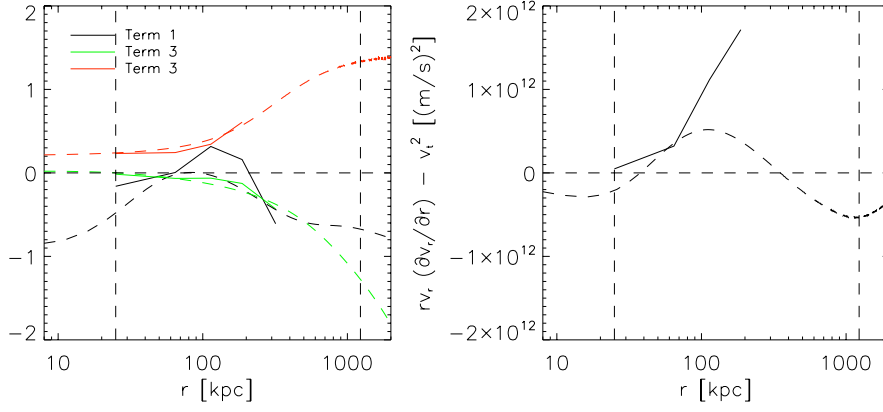


Figure C.3.

C.2 A1914

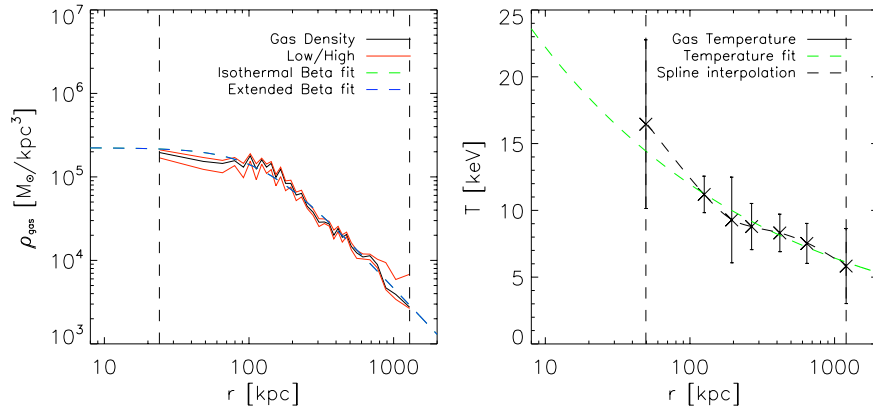


Figure C.4.

C.3. A2218

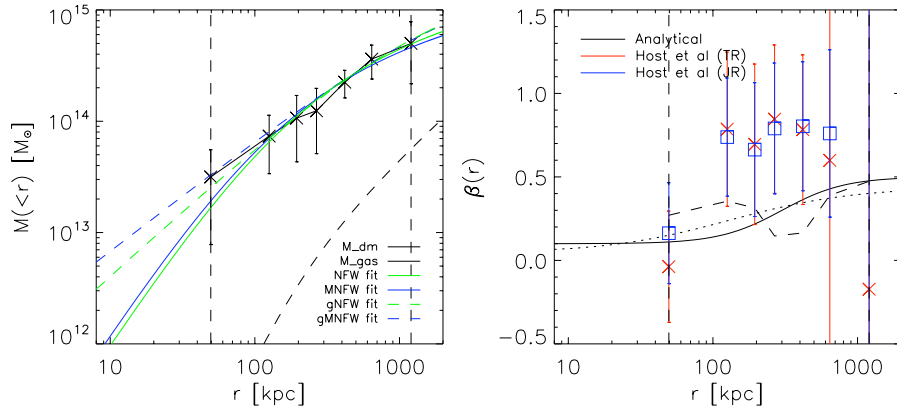


Figure C.5.

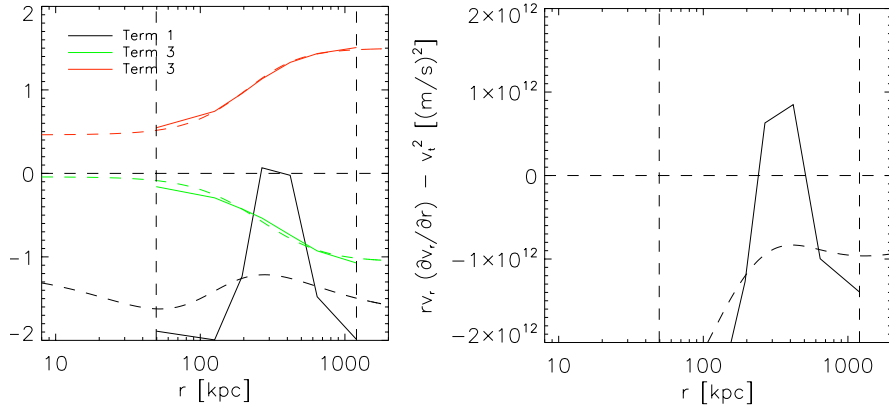
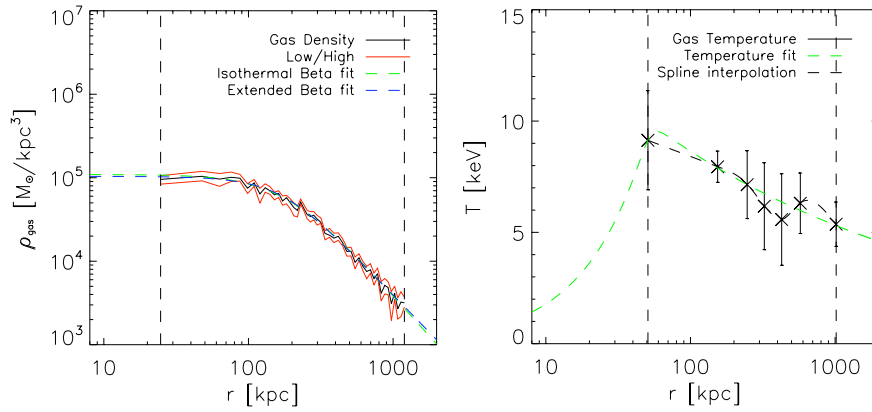


Figure C.6.

C.3 A2218



APPENDIX C. SELECTION OF ANALYSED CLUSTERS

Figure C.7.

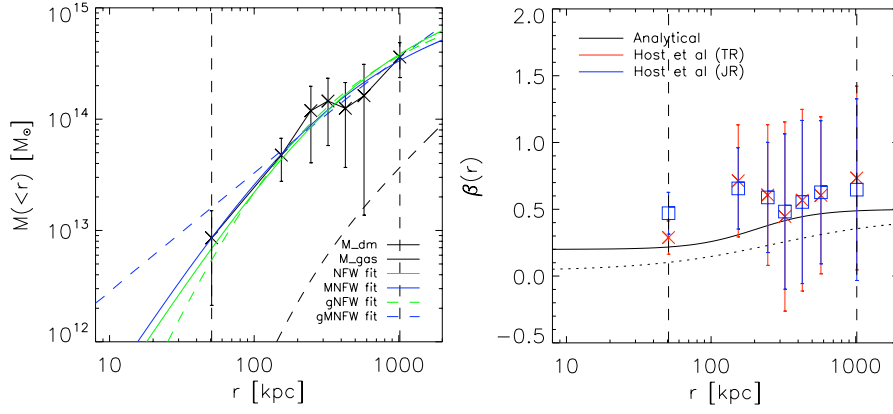


Figure C.8.

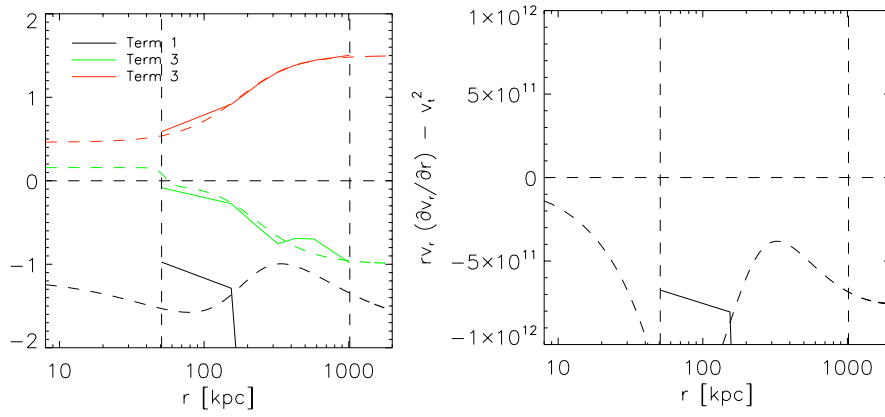


Figure C.9.

# Bibliography

- [1] J. Binney and S. Tremaine. *Galactic Dynamics: Second Edition*. Galactic Dynamics: Second Edition, by James Binney and Scott Tremaine. ISBN 978-0-691-13026-2 (HB). Published by Princeton University Press, Princeton, NJ USA, 2008., 2008.
- [2] R. G. Carlberg, H. K. C. Yee, E. Ellingson, S. L. Morris, R. Abraham, P. Gravel, C. J. Pritchett, T. Smecker-Hane, F. D. A. Hartwick, J. E. Hesser, J. B. Hutchings, and J. B. Oke. The Average Mass Profile of Galaxy Clusters. *ApJ*, 485:L13+, August 1997.
- [3] A. Cavaliere and R. Fusco-Femiano. The Distribution of Hot Gas in Clusters of Galaxies. *A&A*, 70:677–+, November 1978.
- [4] S. Cole and C. Lacey. The structure of dark matter haloes in hierarchical clustering models. *MNRAS*, 281:716–+, July 1996.
- [5] T. Fang, P. J. Humphrey, and D. A. Buote. Rotation and Turbulence of the Hot ICM in Galaxy Clusters. *ArXiv e-prints*, August 2008.
- [6] G. Gilmore, M. Wilkinson, J. Kleyna, A. Koch, W. Evans, R. F. G. Wyse, and E. K. Grebel. Observed Properties of Dark Matter: dynamical studies of dSph galaxies. *Nuclear Physics B Proceedings Supplements*, 173:15–18, November 2007.
- [7] S. H. Hansen and B. Moore. A universal density slope Velocity anisotropy relation for relaxed structures. *New Astronomy*, 11:333–338, March 2006.
- [8] S. H. Hansen and R. Piffaretti. Measuring the dark matter velocity anisotropy in galaxy clusters. *A&A*, 476:L37–L40, December 2007.
- [9] S. H. Hansen and J. Stadel. The velocity anisotropy–density slope relation. *Journal of Cosmology and Astro-Particle Physics*, 5:14–+, May 2006.
- [10] G. Hinshaw, J. L. Weiland, R. S. Hill, N. Odegard, D. Larson, C. L. Bennett, J. Dunkley, B. Gold, M. R. Greason, N. Jarosik, E. Komatsu, M. R. Nolte, L. Page, D. N. Spergel, E. Wollack, M. Halpern, A. Kogut, M. Limon, S. S. Meyer, G. S. Tucker, and E. L. Wright. Five-Year Wilkinson Microwave

## BIBLIOGRAPHY

- Anisotropy Probe (WMAP) Observations: Data Processing, Sky Maps, and Basic Results. *ArXiv e-prints*, March 2008.
- [11] O. Host, S. H. Hansen, R. Piffaretti, A. Morandi, S. Ettori, S. T. Kay, and R. Valdarnini. Measurement of the dark matter velocity anisotropy in galaxy clusters. *ArXiv e-prints*, August 2008.
- [12] W. Hu, D. Scott, and J. Silk. Reionization and cosmic microwave background distortions: A complete treatment of second-order Compton scattering. *Phys. Rev. D*, 49:648–670, January 1994.
- [13] O. Kotov and A. Vikhlinin. Chandra Sample of Galaxy Clusters at  $z = 0.4-0.55$ : Evolution in the Mass-Temperature Relation. *ApJ*, 641:752–755, April 2006.
- [14] L. D. Landau and E. M. Lifshitz. *Fluid mechanics*. Course of theoretical physics, Oxford: Pergamon Press, 1959, 1959.
- [15] S. J. LaRoque, M. Bonamente, J. E. Carlstrom, M. K. Joy, D. Nagai, E. D. Reese, and K. S. Dawson. X-Ray and Sunyaev-Zel’dovich Effect Measurements of the Gas Mass Fraction in Galaxy Clusters. *ApJ*, 652:917–936, December 2006.
- [16] D. E. McLaughlin. The Efficiency of Globular Cluster Formation. *AJ*, 117:2398–2427, May 1999.
- [17] A. Morandi and S. Ettori. Entropy profiles in X-ray luminous galaxy clusters at  $z > 0.1$ . *MNRAS*, 380:1521–1532, October 2007.
- [18] D. Nagai, A. Vikhlinin, and A. V. Kravtsov. Testing X-Ray Measurements of Galaxy Clusters with Cosmological Simulations. *ApJ*, 655:98–108, January 2007.
- [19] J. F. Navarro, C. S. Frenk, and S. D. M. White. The Structure of Cold Dark Matter Halos. *ApJ*, 462:563–+, May 1996.
- [20] J. F. Navarro, A. Ludlow, V. Springel, J. Wang, M. Vogelsberger, S. D. M. White, A. Jenkins, C. S. Frenk, and A. Helmi. The Diversity and Similarity of Cold Dark Matter Halos. *ArXiv e-prints*, October 2008.
- [21] J. R. Peterson and A. C. Fabian. X-ray spectroscopy of cooling clusters. *phys-rep*, 427:1–39, April 2006.
- [22] R. Piffaretti and R. Valdarnini. Total mass biases in X-ray galaxy clusters. *A&A*, 491:71–87, November 2008.
- [23] E. Rasia, G. Tormen, and L. Moscardini. A dynamical model for the distribution of dark matter and gas in galaxy clusters. *MNRAS*, 351:237–252, June 2004.

- [24] C. L. Sarazin. X-ray emission from clusters of galaxies. *Reviews of Modern Physics*, 58:1–115, January 1986.
- [25] V. Springel, C. S. Frenk, and S. D. M. White. The large-scale structure of the Universe. *Nature*, 440:1137–1144, April 2006.
- [26] R. A. Sunyaev, M. L. Norman, and G. L. Bryan. On the Detectability of Turbulence and Bulk Flows in X-ray Clusters. *Astronomy Letters*, 29:783–790, December 2003.
- [27] F. Zwicky. On the Masses of Nebulae and of Clusters of Nebulae. *ApJ*, 86:217–+, October 1937.